Crystalline monolayer graphdiyne synthesized in the MXene interlayer space

Jiaqiang Li
  King Abdullah University of Science and Technology

Haicheng Cao
  King Abdullah University of Science and Technology

Qingxiao Wang
  KAUST

Hui Zhang
  South China University of Technology   https://orcid.org/0000-0003-2269-320X

Qing Liu
  King Abdullah University of Science and Technology

Cailing Chen
  King Abdullah University of Science and Technology

Guanxing Li
  King Abdullah University of Science and Technology

Ya Kong
  College of Chemistry and Molecular Engineering, Peking University

Yichen Cai
  King Abdullah University of Science and Technology

Jie Shen
  King Abdullah University of Science and Technology   https://orcid.org/0000-0002-0263-6454

Zhiping Lai
  King Abdullah University of Science and Technology   https://orcid.org/0000-0001-9555-6009

Ying Wu
  King Abdullah University of Science and Technology

Jin Zhang
  Peking University   https://orcid.org/0000-0003-3731-8859

Yu Han (✉ yu.han@kaust.edu.sa)
  King Abdullah University of Science and Technology   https://orcid.org/0000-0003-1462-1118

Article

Keywords:

Abstract

Graphdiyne (GDY) is an artificial carbon allotrope that is conceptually similar to graphene but composed of *sp*- and *sp*[2]-hybridized carbon atoms. Monolayer GDY (ML-GDY) is predicted to be an ideal two-dimensional (2D) semiconductor material with a wide range of applications. However, its preparation has not been achieved experimentally due to difficulties with synthesis. Here, we report that *in-situ* polymerization of hexaethynylbenzene within the sub-nanometer interlayer space of MXene can effectively prevent out-of-plane growth or vertical stacking of the material, resulting in crystalline ML-GDY. The subsequent exfoliation process successfully yields free-standing GDY monolayers with micrometer-scale lateral dimensions. The fabrication of field-effect transistor on free-standing ML-GDY makes the first measurement of its electronic properties possible. The measured electrical conductivity (5.1×10^3 S m^{-1}) and carrier mobility (231.4 cm^2 V^{-1} s^{-1}) at room temperature are remarkably higher than those of the previously reported multilayer GDY materials. The space-constrained synthesis using layered crystals as templates provides a new strategy for preparing 2D materials with precisely controlled layer numbers and long-range structural order.

Full Text

Graphdiyne (GDY), composed of periodically arranged *sp*- and *sp*[2]-hybridized carbon atoms, is an emerging two-dimensional (2D) material and a novel carbon allotrope.[1-3] Theoretical studies predicted numerous intriguing properties of GDY,[4-9] which can be modulated by tuning the layer number.[10,11] Monolayer GDY (ML-GDY) has attracted particular interest because, unlike zero-bandgap graphene, it exhibits a natural direct bandgap and ultrahigh carrier mobilities on the order of 10^4 cm^2 V^{-1} s^{-1}.[12-14] ML-GDY's excellent semiconducting properties, combined with its extreme thinness, mechanical robustness,[5,15] and inherent nanoporous structure,[12,16] make it a promising material platform for various applications, including flexible electronics,[17,18] energy storage,[19] and molecular-sieving membranes.[20,21] However, due to the difficulty of preparing GDYs with precisely controlled layer numbers and long-range structural order,[11] the theoretical properties of ML-GDY have not been demonstrated experimentally.

Acetylenic homocoupling of hexaethynylbenzene (HEB) is the most common method for the synthesis of GDY,[11,22] and the instability and proneness to side reactions of HEB can be largely addressed by using the Eglinton reaction conditions.[23-25] However, synthesizing ML-GDY remains challenging for two main reasons (Supplementary Fig. 1). First, the alkyne–aryl and alkyne–alkyne single bonds can freely rotate during the coupling of the HEB monomer, leading to out-of-plane random growth of the framework and eventually to the formation of a three-dimensional disordered structure rather than the desired 2D crystalline structure.[17,26,27] Second, free GDY monolayers tend to stack into multilayers *via* van der Waals forces and π–π interactions to lower the surface energy.[28,29]

Several synthetic strategies have been developed to overcome these obstacles. Chemical vapor deposition was used to grow GDY on an Ag substrate to reduce the degrees of freedom of the HEB

monomers. However, only an ill-defined carbonaceous framework was obtained.[30] Confining the monomer coupling to graphene surfaces,[25,29] oil–water or solid–liquid interfaces,[24,31] and electric double layers[17] yielded GDYs with ordered structures, but in the form of multilayers rather than monolayers. A bulk GDY material was used to prepare ML-GDY by mechanical exfoliation.[32] However, given the limited crystallinity of the bulk GDY, as evidenced by the lack of in-plane X-ray diffraction peaks, the as-prepared ML-GDY may be structurally disordered. Moreover, the physical properties of the obtained ML-GDY, which could in turn provide evidence for the material quality, have never been explored. Therefore, the reliable preparation of crystalline ML-GDY remains a synthetic challenge.

This study reports a confined-space synthesis method that enables the preparation of crystalline ML-GDY by using MXene as a template. In this method, HEB monomers diffuse into the periodic interlayer gaps of MXene, where they subsequently polymerize to form the GDY structure in the presence of Cu ions. The sub-nanometer interlayer space of MXene acts as a confinement reactor to effectively suppress the random out-of-plane growth or vertical stacking of GDY. Diffraction, atomic-resolution imaging, and spectroscopic characterizations provide comprehensive and unambiguous evidence for the diffusion, intercalation, and polymerization of HEB monomers within the MXene interlayer space as well as the formation of crystalline ML-GDY therein. The MXene template can be removed by ion intercalation-assisted liquid phase exfoliation to obtain free-standing ML-GDY flakes with micrometer-scale lateral dimensions; this allows the fabrication of field-effect transistor (FET) using ML-GDY for the first time. The ML-GDY device exhibits substantially higher carrier mobility and electrical conductivity than the previously reported multilayer GDY materials.

Growth of ML-GDY in MXene

The preparation of ML-GDY began with selectively etching Al from a dense MAX (Ti_3AlC_2) phase using HF to obtain a layer-structured MXene ($Ti_3C_2T_x$; T: OH or F) phase (Fig. 1a).[33] Note that although MXenes prepared in this way contain mixed OH and F groups at interlayer surfaces,[34] the structural models in this report only display OH terminal groups for simplicity.

Scanning electron microscopy (SEM) images revealed that the as-prepared MXene maintained the lateral dimensions (~10 μm) of the pristine MAX crystals while exhibiting lamellar features along the vertical direction (Supplementary Fig. 2). X-ray photoelectron spectroscopy (XPS) results confirmed the complete removal of Al and the formation of the MXene structure (Supplementary Fig. 3).[35] Powder X-ray diffraction (PXRD) patterns indicated that the conversion of MAX to MXene resulted in a peak shift of the (002) reflection from 9.53° to 8.82° in 2θ, corresponding to an increase in the d spacing from 0.93 to 1.00 nm (Fig. 1b).

The as-prepared MXene powders were dispersed in pyridine to expand their interlayer spaces through molecular intercalation, as evidenced by the increase in the $d_{(002)}$ spacing to 1.30 nm (Supplementary Fig. 4). Next, HEB monomers were introduced into the MXene suspension in pyridine (Fig. 1a). The addition of HEB results in a further increase in the $d_{(002)}$ spacing to 1.37 nm (Fig. 1b and Supplementary Fig. 5),

indicating that HEB molecules could also enter the interlayer space of MXene. The Raman spectrum of the resulting material showed a band at 2107 cm^{-1}, which is characteristic of the alkyne groups in HEB,[25] confirming the intercalation of HEB into MXene (Supplementary Fig. 6). Because the limited interlayer space of MXene cannot accommodate "standing" HEB molecules, the intercalated HEB molecules must adopt a horizontal in-plane configuration (Supplementary Fig. 5). Subsequently, Cu ions were added into the suspension to initiate the Eglinton coupling reaction between HEB monomers (Supplementary Fig. 7). A portion of the Cu ions diffused into the MXene interlayer space, where they initiated the reaction governed by the steric confinement effect to form crystalline ML-GDY. Meanwhile, free Cu ions and HEB monomers in the solution yielded amorphous GDY, which could be largely removed from the GDY-containing MXene by centrifugation due to its much lower density.

The purified GDY-containing MXene (denoted as GDY-MXene) exhibited the same crystal morphology as the MXene template (Supplementary Fig. 8a), indicating that growth of GDY was confined within the interlayer space. The PXRD result revealed that that the *in-situ* growth of GDY resulted in a further increase of the $d_{(002)}$ spacing to 1.54 nm (Fig. 1b). This *d* value corresponds to an available interlayer space of 0.66 nm, which is just enough to accommodate one layer of GDY (Supplementary Fig. 5). Notably, GDY-MXene exhibited a diffraction peak at 2θ of 10.5^o with a *d* spacing of 0.83 nm, which was larger than the $d_{(004)}$ of MXene while perfectly matching the $d_{(100)}$ of the ideal ML-GDY structure (Fig. 1b and Supplementary Fig. 8b). This result indicates that GDY grown in the MXene interlayer space has in-plane structural order (i.e., is crystalline).

Control experiments demonstrated that intercalated solvent (i.e., pyridine) molecules could be removed by vacuum heating, as manifested by the restoration of the interlayer spacing of MXene; likewise, intercalated Cu ions could be removed by washing with dilute HCl solution (Supplementary Fig. 9). In contrast, after the sequential addition of pyridine, HEB, and Cu ions, the significantly expanded interlayer spacing of MXene could not be restored by vacuum heating or HCl washing; this provides additional strong evidence for the formation of an extended GDY framework within MXene.

Scanning transmission electron microscopy (STEM) was used to probe the structural evolution from MAX to MXene and, finally, to GDY-MXene. For each material, high-angle annular dark-field (HAADF) and integrated differential phase-contrast (iDPC)-STEM images were acquired simultaneously to obtain comprehensive structural information; HAADF-STEM can clearly identify the layered structure composed of Ti, whereas iDPC-STEM is more sensitive to the interlayer light elements (Al, O/F, and C).[36] To clearly resolve the atomic columns, the images were all acquired along the [110] zone axis, using specimens prepared with a focused ion beam (Supplementary Fig. 10).

The HAADF-STEM image of MAX showed alternating Ti$_3$ and Al layers with strong and weak contrast, respectively (Fig. 1c). The corresponding iDPC-STEM image showed the Al layers more clearly and even identified the C columns near the Ti columns (Fig. 1c and Supplementary Fig. 11), due to the enhanced contrast of light elements. The HAADF-STEM image shows that, compared with MAX, MXene has larger but empty spaces between Ti$_3$ layers (Fig. 1d). This observation is consistent with the PXRD results and

indicates the complete removal of Al by selective etching. The iDPC-STEM image of MXene confirmed the absence of Al layers, while identifying terminal O/F columns on the surfaces of Ti_3C_2 layers (Fig. 1d and Supplementary Fig. 12). Although the HAADF-STEM image of GDY-MXene was blurred by the electron beam-induced carbon contamination, it revealed a significantly expanded interlayer distance (Fig. 1e), consistent with the PXRD result. Notably, the iDPC-STEM image clearly showed continuous linear contrast between adjacent $Ti_3C_2T_x$ layers (Fig. 1e, 1f), providing the most direct evidence for the successful growth of ML-GDY within the interlayer space of MXene. Figure 1g compares the intensity profiles of the marked regions in the iDPC-STEM images, clearly illustrating the differences in the interlayer structure between the three materials. The large-area STEM image of GDY-MXene demonstrates the uniform distribution of ML-GDY throughout the specimen (Supplementary Fig. 13).

Electron energy loss spectroscopy (EELS) was performed during STEM imaging of GDY-MXene (Fig. 2a). The high-energy resolution (~50 meV) allowed probing different chemical states of carbon species. As shown in Fig. 2b, the C-K edge EELS spectra acquired from the $Ti_3C_2T_x$ layer and the interlayer space (i.e., ML-GDY) differ in the energy-loss near-edge structure (ELNES). Compared with $Ti_3C_2T_x$,[37] the ELNES of ML-GDY shifts slightly to the high energy region, where the primary peak at 285.52 eV and the shoulder peak at 285.93 eV can be attributed to the 1s→π* excitation of carbon−carbon double bonds and the 1s→π* excitation of carbon−carbon triple bonds, respectively.[38] An additional peak is observed at 287.45 eV, which may originate from the C-O bonds generated by the partial oxidation of ML-GDY.[31] The elemental map based on the C-K edge (285.5-287.5 eV) EELS (Fig. 2c) shows stripes with alternating strong and weak intensities, which matches the HAADF-STEM image (Fig. 2a) but with the reversed contrast. This result indicates that the carbon content of the interlayer space is higher than that of the $Ti_3C_2T_x$ layer, demonstrating a high filling rate of ML-GDY in MXene.

To avoid possible interference from GDY formed in solution, a focused ion beam was used to remove the outer surface of a GDY-MXene crystal and then characterized the exposed inner structure using Raman spectroscopy (Supplementary Fig. 14). The obtained Raman spectrum showed a band at 2174 cm^{-1}, which is characteristic of the diacetylenic linkages in the extended network (Fig. 2d).[17,25,39] The absence of the band associated with terminal alkynes at 2107 cm^{-1} indicates a high degree of HEB polymerization, while the appearance of G and D bands provides additional evidence for the formation of GDY within MXene (Fig. 2d). Moreover, the Raman intensity map shows a uniform distribution of diacetylenic linkages over the investigated region (Supplementary Fig. 15). The spectral fitting results of C 1s XPS show that, compared with MXene, GDY-MXene had an additional peak related to the carbon−carbon triple bond[22,24] and a significantly lower C-Ti peak (Fig. 2e). The presence of amorphous carbon with carbon−carbon single and double bonds in MXene has been previously reported and ascribed to contaminants introduced during synthesis.[40] The detection of *sp*-hybridized carbons further evidences the formation of GDY in MXene.

Selected area electron diffraction (SAED) was performed on the periphery of a GDY-MXene crystal, where the crystal was thin enough to allow electron beam penetration. The acquired SAED pattern shows the

coexistence of two sets of hexagonal lattices (Fig. 2f). The lattice composed of strong diffraction spots with small d values can be well indexed based on the [001]-projected MXene structure (a = b = 0.31 nm). The lattice composed of weak diffraction spots with large d values perfectly matches the SAED pattern simulated from an ideal 2D hexagonal ML-GDY structure (a = b = 0.96 nm) (Fig. 2f and Supplementary Fig. 16).[24] The SAED result not only reinforces the conclusion from PXRD that the ML-GDY grown in the interlayer space of MXene is crystalline, but also reveals the 30-degree orientation relationship between ML-GDY and the MXene template (Fig. 2f). It was found that the diffraction spots associated with ML-GDY rapidly disappeared during SAED, suggesting that the structure of ML-GDY is extremely sensitive to electron beam irradiation even under the protection of the MXene template.

Free-standing GDY monolayers

MXene can be easily exfoliated into $Ti_3C_2T_x$ monolayers by sonication in solution (Supplementary Fig. 17),[41] whereas the same treatment cannot decompose GDY-MXene (Supplementary Fig. 18), implying that the growth of ML-GDY led to stronger interlayer interactions. In order to obtain free-standing GDY monolayers from GDY-MXene (Fig. 3a), Li_2SiF_6 was used to facilitate the liquid-phase exfoliation via Li^+ intercalation.[32] The Li^+ intercalation into GDY-MXene increased its interlayer spacing (Supplementary Fig. 19), after which GDY-MXene crystals were decomposed by sonication to form a homogeneous suspension in water (Fig. 3b). The powder collected from the suspension was dispersed on a silicon wafer and then characterized using grazing incidence x-ray diffraction. Three reflections were observed, attributed to the (002) and (004) planes of GDY-MXene after Li^+ intercalation and the (100) planes of ML-GDY, respectively (Fig. 3b). This result demonstrates that the ordered in-plane structure of ML-GDY was preserved during the sonication-assisted exfoliation process, but also indicates that GDY-MXene crystals were not completely exfoliated into GDY and $Ti_3C_2T_x$ monolayers.

Although the obtained powder is a mixture of GDY monolayers, $Ti_3C_2T_x$ monolayers, and residual GDY-MXene sheets, GDY monolayers could be identified by atomic force microscopy (AFM). As shown in Fig. 3c, AFM revealed flakes of different thicknesses, the thinnest being ~0.77 nm (Fig. 3d). Given that the thickness of $Ti_3C_2T_x$ monolayer is about 1.5 nm (Supplementary Fig. 20), flakes with sub-nanometer thicknesses can be unambiguously assigned to GDY monolayers.[32,42,43] Statistics based on AFM observation of 150 GDY monolayers give a lateral dimension distribution of 0.3-2.4 μm centered at 0.75 μm (Supplementary Fig. 21). The Raman spectra collected from different regions of a sub-nanometer-thick flake (pre-identified using AFM) all showed the band characteristic of diacetylenic linkages, confirming its homogeneous GDY structure (Figs. 3e, 3f). The gradually decreasing signal intensity in the Raman spectral series can be attributed to the damaging effect of prolonged laser irradiation (Fig. 3f and Supplementary Fig. 22).

Under transmission electron microscopy, free-standing GDY monolayers can be identified from the weakest image contrast combined with the lack of Ti element determined by EELS or energy-dispersive X-ray spectroscopy (Supplementary Fig. 23). Free-standing GDY monolayers are extremely sensitive to the

electron beam; thus, our attempts to verify their crystallinity using high-resolution TEM imaging were unsuccessful. We compared the EELS spectra collected from a free-standing ML-GDY and the amorphous carbon film of the TEM grid (Fig. 3g, 3h). In the low-loss region, the spectrum of ML-GDY reveals a bandgap of 1.04 eV, which is in good agreement with the theoretical prediction using the first-principles calculations;[44] in contrast, the spectrum of amorphous carbon film showed no bandgap excitation (Fig. 3g). In the core-loss region, ML-GDY exhibits a shoulder peak at 285.91 eV, associated with the 1s→π* excitation of sp carbon bonded carbon–carbon triple bonds,[38] which is not observed in the spectrum of amorphous carbon (Fig. 3h). Moreover, the amorphous carbon has stronger σ* excitation than ML-GDY, suggesting a higher density of sp^3 carbon (Fig. 3h). These results demonstrate that, despite the inevitable partial structural damage during EELS, free-standing ML-GDY displays distinctly different properties from amorphous carbon, including a well-defined bandgap and the presence of sp-hybridized carbon.

Electronic properties of ML-GDY

Semiconducting 2D materials are considered critical for the development of next-generation electronic devices. Theoretical studies indicate that GDY is a semiconductor with electronic properties varying with number of layers. To date, only multilayer GDY materials have been tested.[14,25,29,31,45-49]. The confined-space synthesis reported here enables the preparation of isolated ML-GDY, thus allowing the first measurement of its electronic properties by fabricating a series of FET devices.

The ML-GDY FET was fabricated by depositing Au/Ti on ML-GDY as source and drain terminals and using single-crystal Si as the bottom gate and SiO_2 as the dielectric layer (Fig. 4a and Supplementary Fig. 24). The AFM and Raman characterization results confirmed that the devices were fabricated on ML-GDY (Supplementary Fig. 25). The gate leakage current density of the fabricated ML-GDY FET was as low as 10^{-3} A cm^{-2} at ± 30 V (Supplementary Fig. 26a), confirming the excellent insulating properties of the dielectric SiO_2 layer. The linear I_{ds}–V_{ds} curve measured at 298 K indicated an ohmic-like contact between ML-GDY and electrodes (Fig. 4b), and the calculated conductivity of ML-GDY was $5.1×10^3$ S m^{-1}. The conductivity of ML-GDY increased with the measurement temperature and reached $7.1×10^3$ S m^{-1} at 398 K (Fig. 4c and Supplementary Fig. 26b). This behavior suggests that ML-GDY is a semiconductor while demonstrating its good thermal stability.

The transfer characteristic curve (at V_{ds} = 0.05 V) of the ML-GDY FET showed a spurt in current growth at V_g = ~ 2.5 V. The current reduction during the forward sweep of V_g indicated hole-dominated conduction and thus the p-type nature of ML-GDY (Fig. 4d).[29,31] The output characteristic curves of the device exhibited an obvious evident gate control property (Fig. 4d, inset), which was not observed in previously reported multilayer GDY-based FETs. The carrier mobility of ML-GDY was calculated using the equation μ = $[dI_{ds}/dV_g][L/(WC_g V_{ds})]$,[50] where L is the channel length of the FET, W is the width of ML-GDY (see Fig. 4a), and C_g = 34.5 nF·cm^{-2}. The calculated carrier mobilities from three independent FET devices were 247.1, 213.7, and 233.3 cm^2 V^{-1} s^{-1} (Supplementary Fig. 27 and Supplementary Tab. 1), respectively, with an average value of 231.4 cm^2 V^{-1} s^{-1}.

As summarized in Fig. 4e, ML-GDY exhibits higher electrical conductivity and carrier mobility than previous multilayer GDY materials prepared using various methods (see details in Supplementary Tab. 2). ML-GDY's outstanding electronic properties can be attributed to its high structural order achieved by the confined-space synthesis and single-atom thickness. Nevertheless, the measured carrier mobility of ML-GDY is still considerably lower than theoretical prediction values, which may be due to the partial structural damage of ML-GDY and the introduction of contamination during the fabrication of the FET devices.

Conclusion

High-quality materials with well-defined structures provide the basis for reliable mechanistic and performance studies. Despite numerous research efforts, the synthesis of crystalline monolayer GDY remains a grand challenge, hindering development of its applications. In this work, we demonstrated that the limited interlayer space in MXene can be exploited to facilitate the 2D growth of GDY and avoid vertical stacking. The efficient generation of crystalline GDY monolayers throughout MXene crystals was fully demonstrated by combined diffraction, atomic-resolution imaging, and spectroscopic characterization. Free-standing ML-GDY flakes with micrometer-scale lateral dimensions were obtained from the GDY-MXene composite via ion intercalation-assisted liquid-phase exfoliation, and their retained crystallinity and single-atom thickness were verified. Free-standing ML-GDY allows the fabrication of unprecedented ML-GDY FETs. According to FET measurements, the as-prepared ML-GDY behaves as a *p*-type semiconductor, exhibiting an average carrier mobility of 231.4 cm^2 V^{-1} s^{-1} and a conductivity of 5.1×10^3 S m^{-1} at room temperature, which is superior to various previously reported multilayer GDY materials. The synthetic strategy developed in this work represents a new route to fabricating monolayer 2D structures not viable using conventional synthesis.

Methods
Preparation of MXene

The MXene material was prepared from a commercial MAX (Ti_3AlC_2) phase using an established method.[33] In a typical procedure, 1 g of MAX was added to an argon-filled Teflon reactor, followed by 20 mL of HF solution (30%) under stirring, continued at room temperature for 22 h. The sediment was collected by centrifugation (10 min, 8000 rpm) and washed by deionized H_2O repeatedly until the pH of the supernatant reached neutral. The obtained powder (MXene) was freeze-dried.

Synthesis of HEB

Tetrabutylammonium fluoride (1 M in THF, 0.5 mL) was added to 20 mL of THF containing 50 mg of hexakis[(trimethylsilyl)-ethynyl]benzene under an argon atmosphere, and the mixture was stirred at 0 ^{o}C for 15 min. The mixture was then washed twice with 50 mL of saturated NaCl solution, dried over anhydrous $MgSO_4$, and filtered. The solvent was evaporated, and the residue was redissolved in 20 mL of

EtOAc. The solution was purified by chromatography using a short silica gel column (length: 2 cm; diameter: 2.5 cm). Finally, the solvent was removed by evaporation, and the obtained white solid (HEB) was dissolved in 5 mL of dichloromethane (DCM). Note that since HEB is unstable at room temperature and sensitive to oxygen, all these procedures should be performed quickly in the dark and the DCM solution of HEB should be stored at 4°C under argon. The ^{1}H NMR (400 MHz, DMSO) and ^{13}C NMR (125 MHz, DMSO) spectra of HEB are presented in Supplementary Fig. 28.

Growth of ML-GDY in MXene

MXene powder (50 mg) was dispersed in 20 mL of pyridine under an argon atmosphere, and the obtained suspension was ultrasonicated for 5 mins. Then, 5 mL of HEB solution in DCM prepared in the previous step was dropwise added into the MXene suspension, and the resulting mixture was stirred at 0°C for 5 h. Next, 5 mL of pyridine containing 25 mg of $Cu(OAc)_2$ was added. After 24 h of reaction at room temperature under static conditions, the supernatant was carefully removed and the solid was collected by filtration and washed by pyridine, *N,N*-dimethylformamide, and water successively. To remove residual Cu, the solid was immersed in 10 mL of 0.5 M HCl for 10 h. Finally, the solid was collected by filtration, washed thoroughly with deionized water and ethanol, and air dried. The obtained black composite is denoted as GDY-MXene.

Preparation of free-standing ML-GDY

Free-standing GDY monolayers were prepared using ion intercalation-assisted liquid phase exfoliation. Typically, 50 mg of Li_2SiF_6 was added to 20 mL of water, followed by 20 mg of GDY-MXene. The mixture was continuously stirred at 25°C for 48 h under an inter gas atmosphere to ensure complete intercalation of Li into GDY-MXene. The Li-intercalated GDY-MXene was collected by centrifugation (8000 rpm for 15 min) and washed thoroughly with deionized water to remove the residual Li_2SiF_6. The obtained solid was dispersed in 50 mL of H_2O and then ultrasonicated (power: 1000 W) at 0°C for 30 min. The resulting homogenous suspension contained GDY monolayers, $Ti_3C_2T_x$ monolayers, and incompletely exfoliated GDY-MXene sheets.

Fabrication and measurements of ML-GDY FETs

A 1 × 1 cm SiO_2 (100 nm)/Si (0.5 mm) substrate was treated with O_2 plasma for 10 s. Then, 10 μL of the suspension containing GDY monolayers (i.e., the suspension that had undergone the exfoliation process) was added dropwise on the SiO_2/Si substrate. After air drying, the substrate was kept under vacuum at 60 °C for 2 h. Then, electrode patterns were fabricated on ML-GDY flakes using electron beam lithography. Gold and titanium stacks with thicknesses of 100 and 10 nm, respectively, were deposited as electrodes by sputter coating and lift-off procedures to form a ML-GDY FET with a 1 μm channel length. A semiconductor analyzer (Keithley 4200SCS) was used to determine the conductivity and transfer characteristics of the ML-GDY FET. The $I-V$ curves at different temperatures were measured using a Keithley 4200SCS with a heating stage (IKA RCT 5 digital).

The calculation of mobility is based on the following equations:

$$\mu = \left[\frac{dI_{ds}}{dV_g} \right] \left[\frac{L}{W C_g V_{ds}} \right]$$

$$C_g = \frac{\epsilon_r \epsilon_0}{d}$$

where L is the channel length of the FET, W is the width of the ML-GDY flake, d is the thickness of the SiO$_2$ layer, ε_r is the dielectric constant of SiO$_2$, and ε_0 is the vacuum dielectric constant.

The calculation of conductivity is based on the following equation:

$$\delta = \frac{L}{RWH}$$

where L and R are the channel length and resistance of the ML-GDY FET, respectively; W and H are the width and thickness of ML-GDY, respectively.

Declarations

Data availability

The data supporting the findings of this study are available within the paper and Supplementary Information. Source data are provided with this paper.

Acknowledgements

Author contributions

Y.H. and J.Z. conceived and designed the experiments. J.L., Q.L., and Y.C prepared the MXene material. J.L., Q.L., Y.K, and J.S. synthesized GDY-MX and performed spectroscopic characterizations. H.C. and J.L. fabricated FET devices and measured the electronic properties of ML-GDY. Q.W., H.Z., J.L., C.C, and G.L. acquired high-resolution electron microscopy images and performed EELS spectra. All authors were involved in the analysis and discussion of the results. Y.H. and J.L. wrote the manuscript and all authors commented on the manuscript.

## Competing interests

The authors declare no competing interests.

References

1. Huang, C. *et al.* Progress in research into 2D graphdiyne-based materials. *Chem. Rev.* **118**, 7744-7803 (2018).

2. Hirsch, A. The era of carbon allotropes. *Nat. Mater.* **9**, 868-871 (2010).

3. Jia, Z. Y. *et al.* Synthesis and properties of 2D carbon—graphdiyne. *Accounts Chem. Res.* **50**, 2470-2478 (2017).

4. Pan, L. D., Zhang, L. Z., Song, B. Q., Du, S. X. & Gao, H. J. Graphyne- and graphdiyne-based nanoribbons: Density functional theory calculations of electronic structures. *Appl. Phys. Lett.* **98**, 173102 (2011).

5. Yang, Y. & Xu, X. Mechanical properties of graphyne and its family – A molecular dynamics investigation. *Comput. Mater. Sci.* **61**, 83-88 (2012).

6. Cui, H. J., Sheng, X. L., Yan, Q. B., Zheng, Q. R. & Su, G. Strain-induced Dirac cone-like electronic structures and semiconductor-semimetal transition in graphdiyne. *Phys. Chem. Chem. Phys.* **15**, 8179-8185 (2013).

7. Ivanovskii, A. L. Graphynes and graphdyines. *Prog. Solid State Chem.* **41**, 1-19 (2013).

8. Jalili, S., Houshmand, F. & Schofield, J. Study of carrier mobility of tubular and planar graphdiyne. *Appl. Phys. A* **119**, 571-579 (2015).

9. Zheng, Y. *et al.* Intrinsic magnetism of graphdiyne. *Appl. Phys. Lett.* **111**, 033101 (2017).

10. Zheng, Q. *et al.* Structural and electronic properties of bilayer and trilayer graphdiyne. *Nanoscale* **4**, 3990-3996 (2012).

11. Kong, Y. *et al.* Bridging the gap between reality and ideality of graphdiyne: The advances of synthetic methodology. *Chem* **6**, 1933-1951 (2020).

12. Li, Y., Xu, L., Liu, H. & Li, Y. Graphdiyne and graphyne: from theoretical predictions to practical construction. *Chem. Soc. Rev.* **43**, 2572-2586 (2014).

13. Long, M., Tang, L., Wang, D., Li, Y. & Shuai, Z. Electronic structure and carrier mobility in graphdiyne sheet and nanoribbons: Theoretical predictions. *ACS Nano* **5**, 2593-2600 (2011).

14. Chen, J., Xi, J., Wang, D. & Shuai, Z. Carrier mobility in graphyne should be even larger than that in graphene: A theoretical prediction. *J. Phys. Chem. Lett.* **4**, 1443-1448 (2013).

15. Pari, S., Cuellar, A. & Wong, B. M. Structural and electronic properties of graphdiyne carbon nanotubes from large-scale DFT calculations. *J. Phys. Chem. C* **120**, 18871-18877 (2016).

16. Bartolomei, M. *et al.* Penetration barrier of water through graphynes' Pores: First-principles predictions and force field optimization. *J. Phys. Chem. Lett.* **5**, 751-755 (2014).

17. Li, J. *et al.* Synthesis of wafer-scale ultrathin graphdiyne for flexible optoelectronic memory with over 256 storage levels. *Chem* **7**, 1284-1296 (2021).

18. Zhang, Y. *et al.* Graphdiyne-based flexible photodetectors with high responsivity and detectivity. *Adv. Mater.*, 2001082 (2020).

19. Wang, N. *et al.* Graphdiyne-based materials: preparation and application for electrochemical energy storage. *Adv. Mater.* **31**, 1803202 (2019).

20. Qiu, H., Xue, M., Shen, C., Zhang, Z. & Guo, W. Graphynes for water desalination and gas separation. *Adv. Mater.* **31**, 1803772 (2019).

21. Fang, L. & Cao, Z. Isoelectronic doping and external electric field regulate the gas-separation performance of graphdiyne. *J. Phys. Chem. C* **124**, 2712-2720 (2020).

22. Zhou, J. *et al.* Synthesis of graphdiyne nanowalls using acetylenic coupling reaction. *J. Am. Chem. Soc.* **137**, 7596-7599 (2015).

23. Eglinton, G. & Galbraith, A. "Cyclic dyines," *Chem. Ind.* 736–737 (1956).

24. Matsuoka, R. *et al.* Crystalline graphdiyne nanosheets produced at a gas/liquid or liquid/liquid interface. *J. Am. Chem. Soc.* **139**, 3145-3152 (2017).

25. Gao, X. *et al.* Ultrathin graphdiyne film on graphene through solution phase van der Waals epitaxy. *Sci. Adv.* **4**, eaat6378 (2018).

26. Sakamoto, J., van Heijst, J., Lukin, O. & Schluter, A. D. Two-dimensional polymers: just a dream of synthetic chemists? *Angew. Chem. Int. Ed.* **48**, 1030-1069 (2009).

27. Zhou, J., Li, J., Liu, Z. & Zhang, J. Exploring approaches for the synthesis of few-layered graphdiyne. *Adv. Mater.* **31**, 1803758 (2019).

28. Colson, J. W. *et al.* Oriented 2D covalent organic framework thin films on single-layer graphene. *Science* **332**, 228-231 (2011).

29. Zhou, J. *et al.* Synthesis of ultrathin graphdiyne film using a surface template. *ACS Appl. Mater. Inter.* **11**, 2632–2637 (2018).

30. Liu, R. *et al.* Chemical vapor deposition growth of linked carbon monolayers with acetylenic scaffoldings on silver foil. *Adv. Mater.* **29**, 1604665 (2017).

31. Yin, C. *et al.* Catalyst-free synthesis of few-layer graphdiyne using a microwave-induced temperature gradient at a solid/liquid interface. *Adv. Funct. Mater.* **30**, 2001396 (2020).

32. Yan, H. *et al.* High-yield and damage-free exfoliation of layered graphdiyne in aqueous phase. *Angew. Chem. Int. Ed.* **58**, 746-750 (2019).

33. Lukatskaya, M. R. *et al.* Cation intercalation and high volumetric capacitance of two-dimensional titanium carbide. *Science* **341**, 1502-1505 (2013).

34. Naguib, M. *et al.* Two-dimensional nanocrystals produced by exfoliation of Ti_3AlC_2. *Adv. Mater.* **23**, 4248-4253 (2011).

35. Mashtalir, O. *et al.* Intercalation and delamination of layered carbides and carbonitrides. *Nat. Commun.* **4**, 1716 (2013).

36. Yucelen, E., Lazic, I. & Bosch, E. G. T. Phase contrast scanning transmission electron microscopy imaging of light and heavy atoms at the limit of contrast and resolution. *Sci. Rep.* **8**, 2676 (2018).

37. Magne, D., Mauchamp, V., Celerier, S., Chartier, P. & Cabioc'h, T. Site-projected electronic structure of two-dimensional Ti_3C_2 MXene: the role of the surface functionalization groups. *Phys. Chem. Chem.*

Phys. **18**, 30946-30953 (2016).

38. Zhong, J. *et al.* Electronic structure of graphdiyne probed by X-ray absorption spectroscopy and scanning transmission X-ray microscopy. *J. Phys. Chem. C* **117**, 5931-5936 (2013).

39. Zhang, S. *et al.* Raman spectra and corresponding strain effects in graphyne and graphdiyne. *J. Phys. Chem. C* **120**, 10605-10613 (2016).

40. Natu, V. *et al.* A critical analysis of the X-ray photoelectron spectra of $Ti_3C_2T_z$ MXenes. *Matter* **4**, 1224-1251 (2021).

41. Zhang, J. *et al.* Scalable manufacturing of free-standing, strong $Ti_3C_2T_x$ mxene films with outstanding conductivity. *Adv. Mater.* **32**, 2001093 (2020).

42. Wang, M. *et al.* Single-crystal, large-area, fold-free monolayer graphene. *Nature* **596**, 519-524 (2021).

43. Toh, C. T. *et al.* Synthesis and properties of free-standing monolayer amorphous carbon. *Nature* **577**, 199-203 (2020).

44. Luo, G. *et al.* Quasiparticle energies and excitonic effects of the two-dimensional carbon allotrope graphdiyne: Theory and experiment. *Phys. Rev. B* **84**, 2250-2262 (2011).

45. Qian, X. *et al.* Self-catalyzed growth of large-area nanofilms of two-dimensional carbon. *Sci. Rep.* **5**, 7756 (2015).

46. Li, Y. *et al.* Light and heat triggering modulation of the electronic performance of a graphdiyne-based thin film transistor. *J. Phys. Chem. Lett.* **11**, 1998-2005 (2020).

47. Zhao, F. *et al.* In situ growth of graphdiyne on arbitrary substrates with a controlled-release method. *Chem. Commun.* **54**, 6004-6007 (2018).

48. Li, G. *et al.* Architecture of graphdiyne nanoscale films. *Chem. Commun.* **46**, 3256-3258 (2010).

49. Zuo, Z. *et al.* A facile approach for graphdiyne preparation under atmosphere for an advanced battery anode. *Chem. Commun.* **53**, 8074-8077 (2017).

50. Radisavljevic, B., Radenovic, A., Brivio, J., Giacometti, V. & Kis, A. Single-layer MoS_2 transistors. *Nat. Nanotechnol.* **6**, 147-150 (2011).
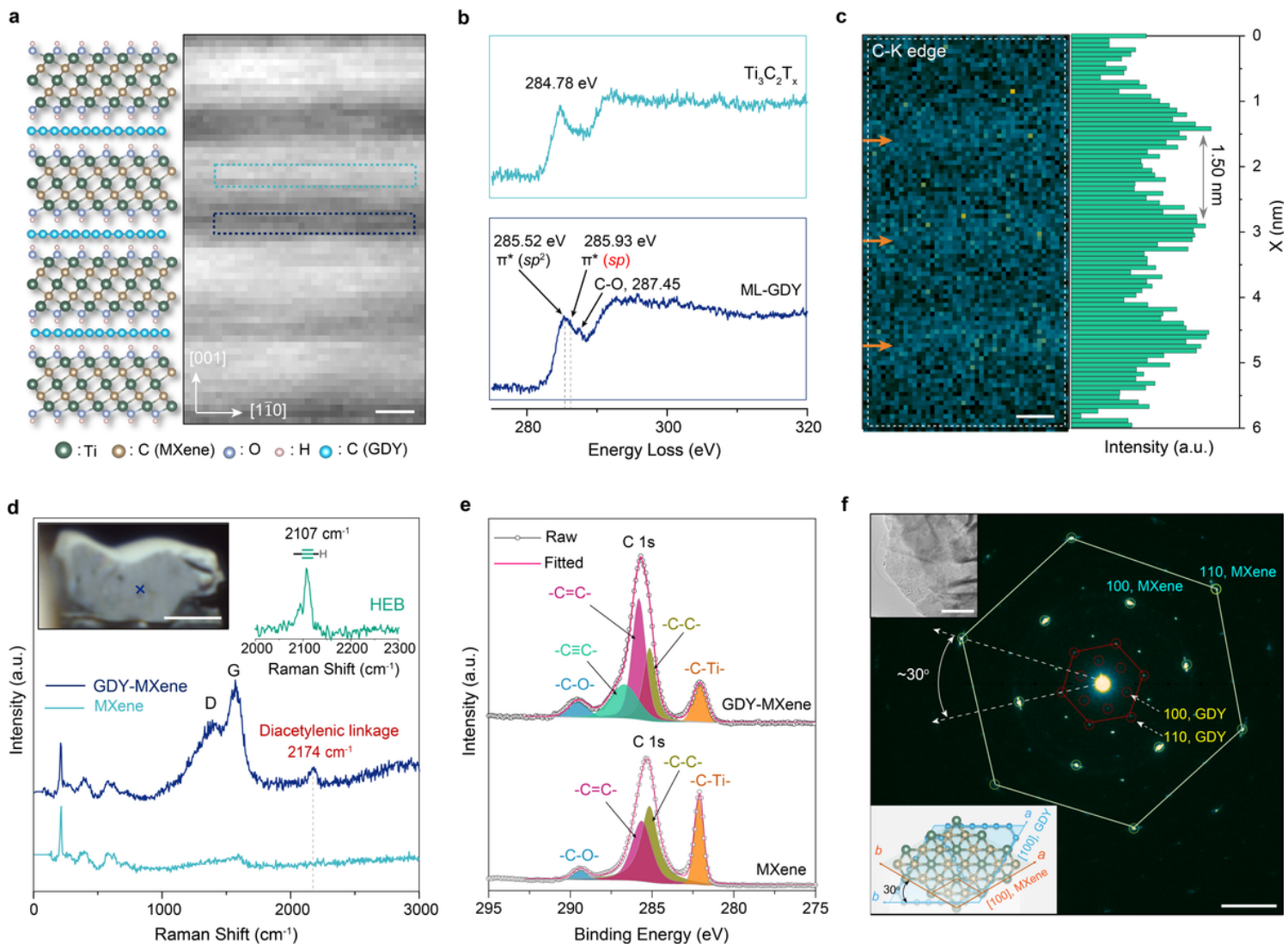
Figures
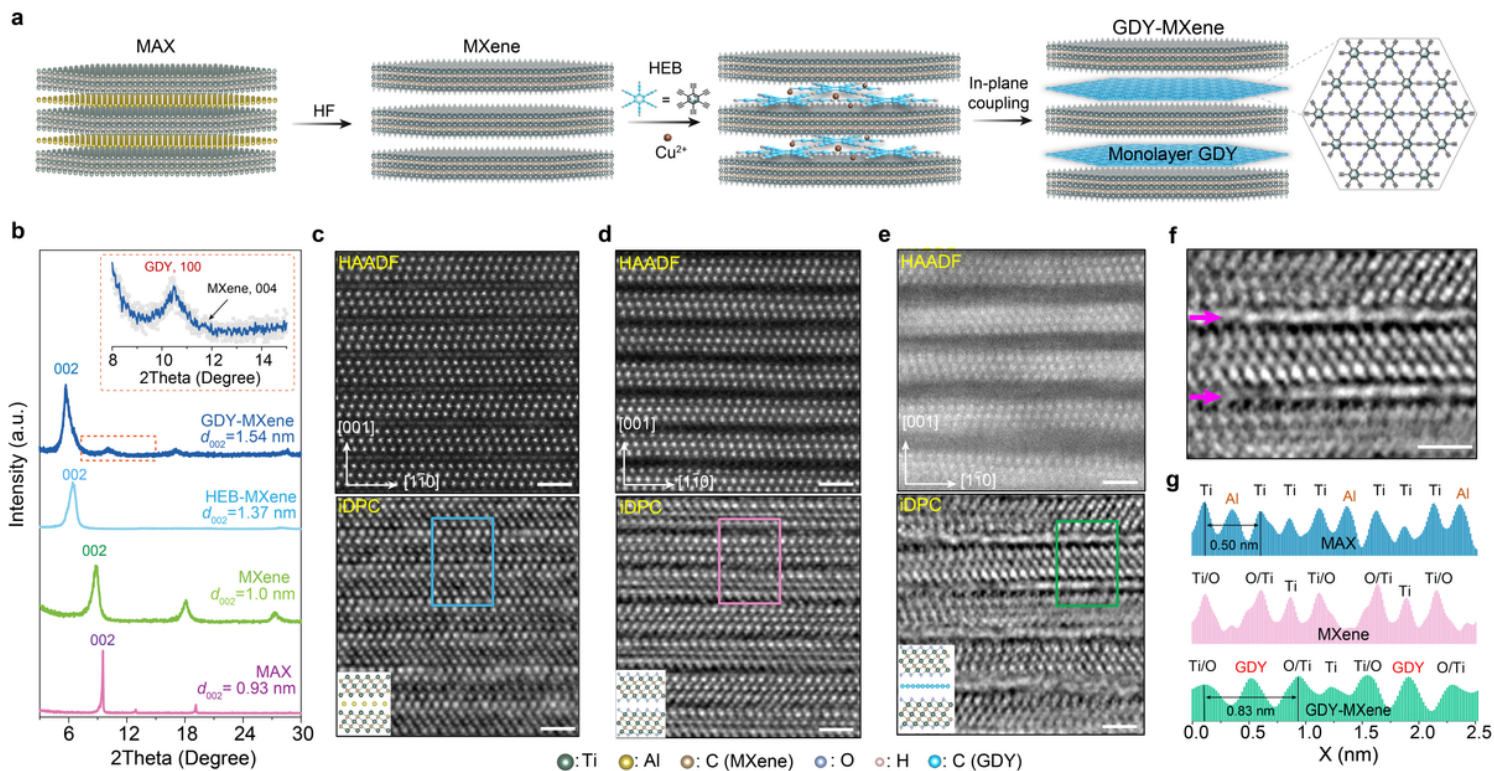
Figure 1

Growth of GDY monolayers in MXene. a, Schematic illustration of the process for growing GDY monolayers in the interlayer space of MXene. b, Experimental PXRD patterns of MAX, MXene, HEB-intercalated MXene (HEB-MXene), and GDY-MXene. The inset is a magnified view of the selected region in the PXRD pattern of GDY-MXene, showing the in-plane (100) reflection of GDY. c-e, Atomic-resolution HAADF-STEM (upper panel) and iDPC-STEM (lower panel) images of MAX (c), MXene (d), and GDY-MXene (e) acquired along the [110] zone axis. Insets are the corresponding structural models. f, Magnified iDPC-STEM image of GDY-MXene. Arrows indicate GDY monolayers grown in the interlayer space of MXene. g, Image intensity profiles extracted from the marked areas in (c), (d), and (e). Atomic types of the identified columns are labelled, revealing the distinctly different interlayer structures of the three materials. All scale bars represent 2 nm.
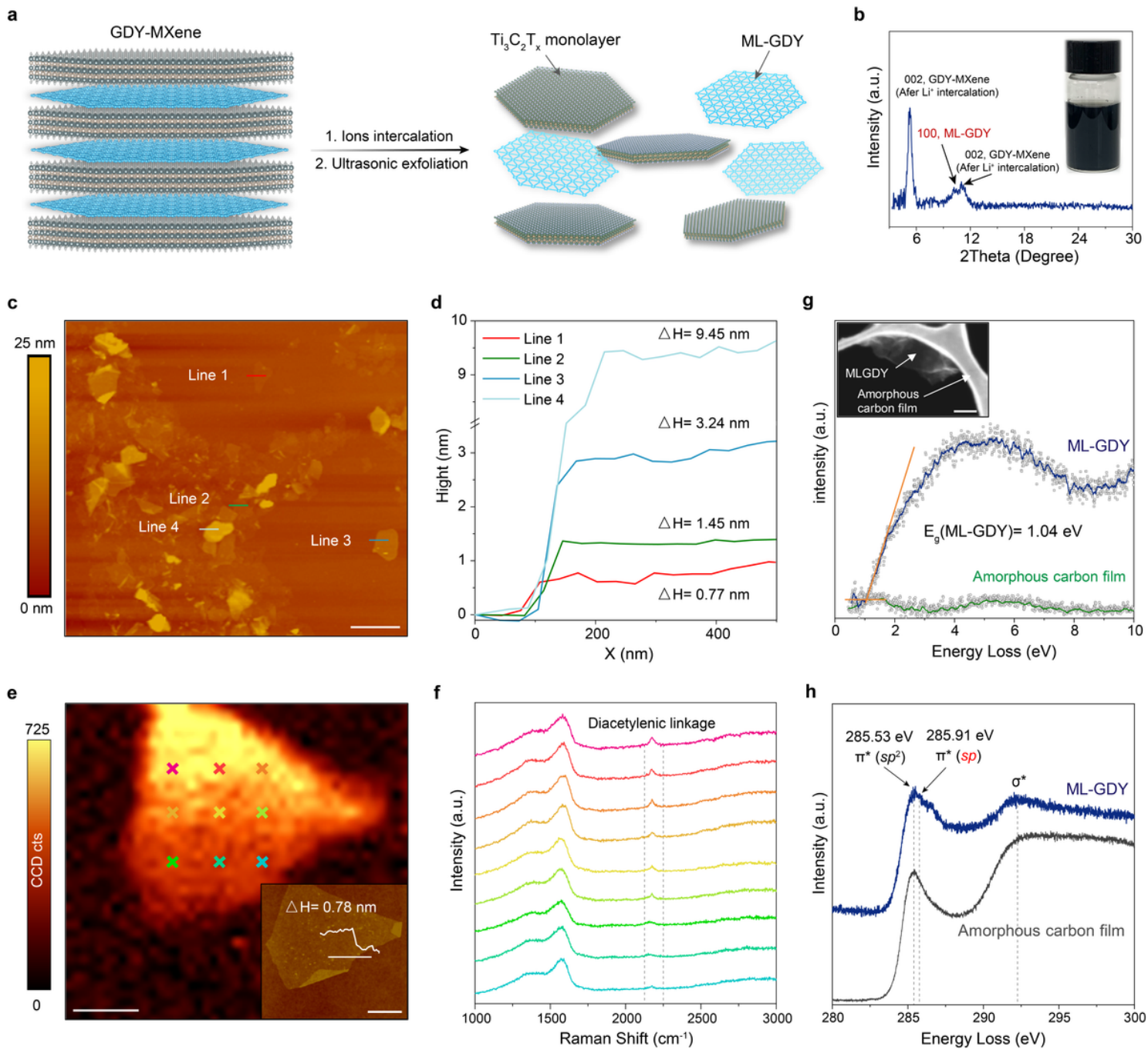
Figure 2

Spectroscopic and structural characterization of GDY-MXene. a, Structural model (left) and annular dark field-STEM image (right) of GDY-MXene along the [110] zone axis. The scale bar represents 0.5 nm. b, The C-K edge EELS spectra collected from the $Ti_3C_2T_x$ layer (upper) and interlayer space (lower) in GDY-MXene, as marked in (a). c, Elemental map (left) and intensity profile (right) based on the C-K edge (285.5-287.5 eV) EELS spectra collected from the region shown in (a), indicating a high carbon content in the interlayer space. The scale bar represents 0.5 nm. d, Raman spectra of MXene and GDY-MXene. The left inset is an optical microscopy image of a GDY-MXene crystal etched using a focused ion beam to expose the internal structure. The cross mark indicates where the Raman spectrum was collected. The scale bar represents 5 μm. The right inset shows the Raman spectrum of HEB for comparison. e, High-resolution C1s XPS spectra of MXene and GDY-MXene. f, SAED pattern of GDY-MXene, showing two sets of hexagonal lattices that can be assigned to MXene and GDY structures with a 30° orientation relationship. The scale bar represents 2 1/nm. The upper inset is the TEM image of the GDY-MXene crystal from which the SAED pattern was acquired, in which the scale bar represents 1 μm. The lower inset is a structural model illustrating the orientation relationship between ML-GDY and MXene.
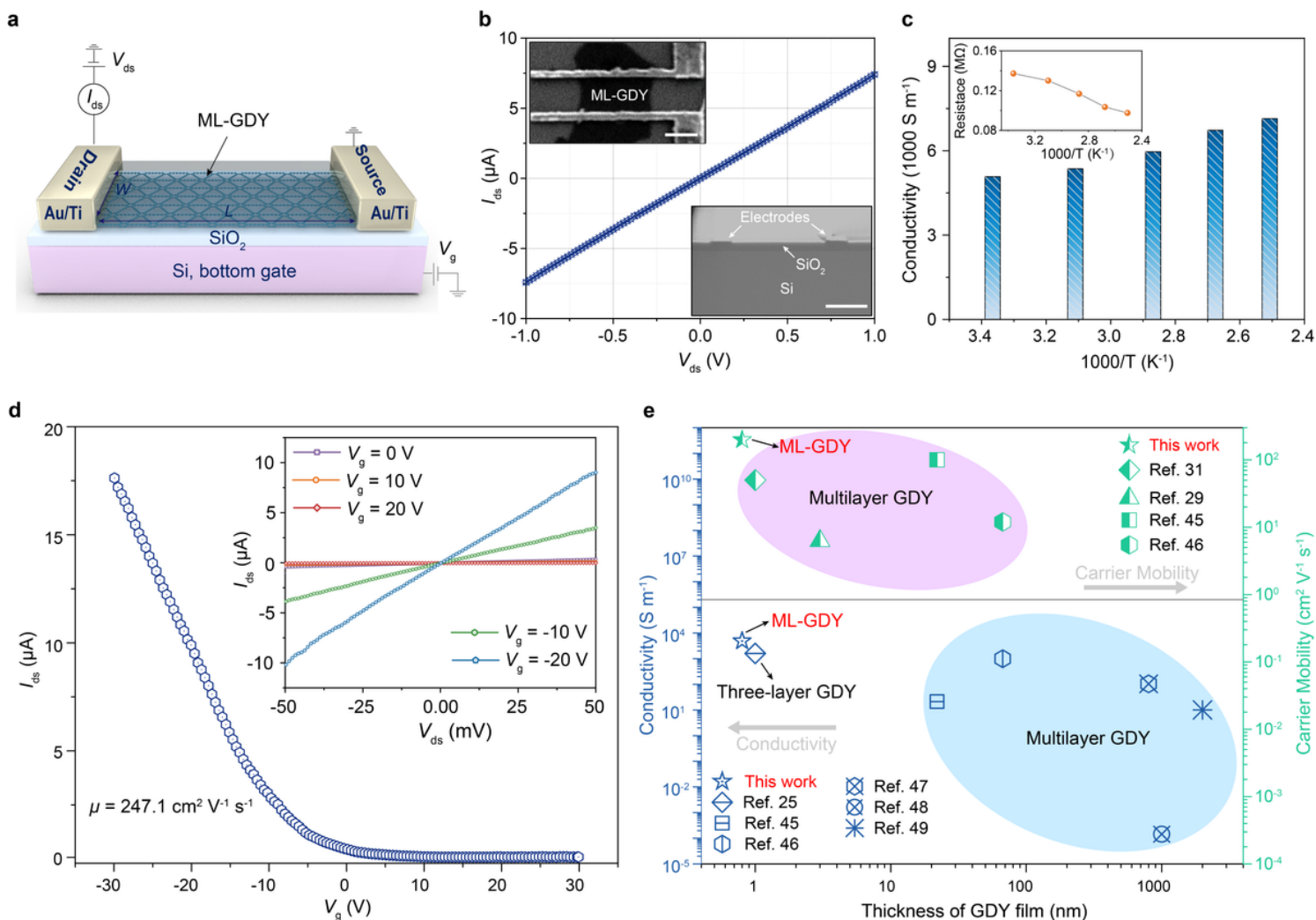
Figure 3

Preparation and characterization of free-standing ML-GDY. a, Schematic illustration showing preparation of free-standing ML-GDY from GDY-MXene by ion intercalation-assisted exfoliation. b, Grazing incidence x-ray diffraction pattern of the exfoliated GDY-MXene powder. Inset is a photograph of the suspension obtained after the exfoliation process. c, AFM image of the exfoliated GDY-MXene powder, showing a mixture of flakes of different thicknesses. The scale bar represents 2 μm. d, AFM height profiles of the four labelled flakes in (c). e, Raman intensity map of a ML-GDY flake based on the signals ranging from 2120 to 2230 cm^{-1}. Inset is the corresponding AFM image. The scale bars represent 500 nm. f, Raman spectra collected from the marked positions in (e). g and h, Low-loss (g) and core-loss (h) EELS spectra

collected from free-standing ML-GDY and the amorphous carbon film of the TEM grid. The inset in g is a STEM image of the area where the EELS spectra were collected. The scale bar represents 200 nm.

Figure 4

Fabrication and measurements of ML-GDY FETs. a, Schematic illustration of the structure of the ML-GDY FET device. b, I_{ds}–V_{ds} characteristic of ML-GDY measured at 298 K. The upper left inset is a top-view SEM image of the device and bottom right is a cross-sectional HAADF-STEM image of the device. Scale bars represent 500 nm. c, Conductivities and resistances (inset) of ML-GDY as an inverse function of temperature. d, Transport characteristic curve of the ML-GDY FET at V_{ds} = 0.05 V. The inset shows output characteristic curves of ML-GDY FET recorded under various V_g biases from −20 to 20 V. e, Comparisons of ML-GDY with previously reported multilayer GDY materials in conductivity and carrier mobility.

Supplementary Files

This is a list of supplementary files associated with this preprint. Click to download.

- SupplementaryMaterials.pdf